

Wavelength selection of rolling-grain ripples in the laboratory

Germain Rousseaux,^{1,*} Alexandre Stegner,^{2,†} and José Eduardo Wesfreid^{1,‡}

¹*Physique et Mécanique des Milieux Hétérogènes, UMR 7636 CNRS-ESPCI, 10, Rue Vauquelin, 75231 Paris Cedex 05, France*

²*Laboratoire de Météorologie Dynamique, ENS, 24, Rue Lhomond, 75005 Paris, France*

(Received 16 June 2003; revised manuscript received 23 October 2003; published 31 March 2004)

We have performed an experimental study, at very high resolution, of the wavelength selection and the evolution of rolling-grain ripples. A clear distinction is made between the flat sand bed instability and the ripple coarsening. The observation of the initial wavelength for the rolling-grain ripples is only possible close to the threshold for movement which imposes a constraint on the parameters. Moreover, we have proposed a law for the selection of the unstable wavelength under the latter constraint. Our results suggest that the initial wavelength depends on the amplitude of oscillation, the grain diameter, and the Stokes layer. Besides, during the coarsening, we observe no self-similarity of the ripple shape and for few cases a logarithmic growth of the wavelength.

DOI: 10.1103/PhysRevE.69.031307

PACS number(s): 45.70.-n, 47.20.-k, 47.54.+r

A flat particle bed submitted to an oscillatory viscous flow is generally unstable. This leads to the formation of ripples. Such patterns are encountered in coastal regions where sea waves in shallow water induce a back and forth fluid motion on sandy sea beds. These ripples follow three dynamical stages. Initially, the rolling of individual grains on the flat bed leads to the formation of small patterns, called *rolling-grain ripples* [1]. Linear stability analysis is used to predict the wavelength selection in this first stage [2,3]. In a second stage, the rolling grain ripples undergo a coarsening process which increases strongly both the height and the wavelength of the patterns [4]. If we wait long enough, the system evolves to a final *vortex ripples* state [5–7]. As far as laboratory experiments as well as field measurements are concerned, the first and second stages are generally mixed together and the rapid coarsening of ripples can mask the first unstable wavelength of the flat sand bed. The aim of this work is to differentiate the wavelength measurements during these two dynamical stages in order to clarify the governing mechanism close to the onset of ripple formation. We focused on the wavelength selection of initial rolling-grain ripples, their temporal evolution during the coarsening and we characterized their morphology with great accuracy.

In order to analyze the dynamics of a granular sand bed under an oscillatory viscous flow, we introduce four length scales, namely: the amplitude of fluid oscillation A , the Stokes layer thickness $\delta = \sqrt{\nu/(\pi f)}$, the grain diameter d , and the viscous length $l_v = (\rho_f \nu^2 / (\rho_s - \rho_f) g)^{1/3}$, where f is the frequency of oscillation, ν the kinematic viscosity, ρ_s the grains density, and ρ_f the fluid density. The wavelength selection of vortex ripples state is well known. The sand bed deformation is mainly controlled by boundary layer separation and generation of vortical structures at the ripple crest [1,8], and the equilibrium wavelength is simply proportional to A [1,8]. For rolling-grain ripples, the situation is more complex. On one hand, the size of the steady recirculating

cells, which appear above an infinitely small rippled bottom, could scale both with δ and A [9–12]. On the other hand, the sediment transport depends on the granular properties of the sand bed and is influenced by d and l_v . Although rolling-grain ripples have been studied in laboratory for a long time, experimental data present strong dispersion and the wavelength selection with respect to δ , A , and d remains unclear.

As in other recent experiments on sand ripples induced by an oscillating flow [5,6] or by a steady shear flow [13,14], we used a cylindrical geometry to avoid end effects which could influence the destabilization of the sand bed. The annular channel (shown in Fig. 1 in Ref. [15]) is made of an inner black cylinder having a radius $R_1 = 6.925$ cm linked with an outer Plexiglas cylinder of radius $R_2 = 7.70$ cm. This leads to a narrow gap width $a = 0.75$ cm which limits the development of various two-dimensional patterns [17]. We closed the top and the bottom of the cell by rigid disks fixed to the cylinders. At the bottom of the cell we introduced a flat layer (4–7 cm height) of monodisperse spherical glass particle having a density $\rho_s = 2.5$ g cm⁻³ while the whole cell (29 cm height) is filled with water. The mean grain diameter d was varied from 65 μ m to 335 μ m. The displacement $D(t) = A \cos(2\pi ft)$ of the annular channel is controlled by the frequency f and the amplitude A of the oscillation. On one hand, the frequency is sufficiently high (from 0.2 Hz to 2 Hz) to keep the Stokes layers relative to the cylinders (from 400 μ m to 1200 μ m) smaller than the gap whereas the third Stokes layer at the sand-fluid interface is larger than the grain size. Hence, the fluid in the center of the channel remains at rest, in the laboratory frame, while the sand bed oscillates. On the other hand, the acceleration of the oscillation is sufficiently low (from 0.5 cm to 30 cm for the amplitude) to neglect the inertial force $\rho_s a_i$ [with $a_i = A(2\pi f)^2$] with respect to the effective gravity force acting on the sand grain $(\rho_s - \rho_f)g$. We used $g^* = g(\rho_s - \rho_f)/\rho_s$ for the reduced gravity of the sediment. The acceleration parameter $\Gamma_s = a_i/g^*$ remained small, between 0.05 and 0.17, for almost all the cases we studied. The dynamical behavior of the sand layer is then expected to be identical whether the sand bed is stationary and the fluid moving, or the fluid stationary and the bed moving.

*Electronic address: germain@pmmh.espci.fr

†Electronic address: wesfreid@pmmh.espci.fr

‡Electronic address: stegner@lmd.ens.fr

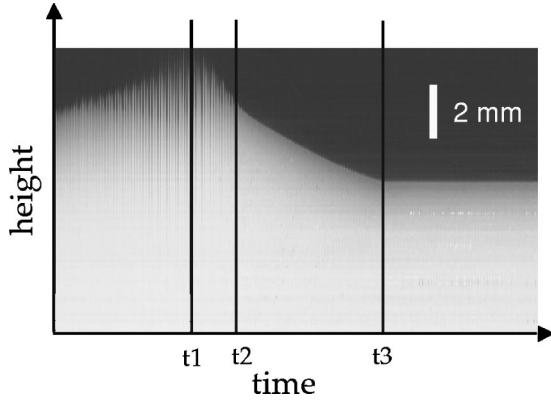


FIG. 1. (Color online) Evolution of the sand height during the flattening procedure. In a first step ($t < t_1$), there is a fluidization ($A = 3$ cm, $f = 3$ Hz, $\Gamma_{sand} = 1.8$) of the upper sand layer. Then, the amplitude is strongly reduced ($A = 0.1$ cm, $f = 3$ Hz, $\Gamma_{sand} = 0.06$) and a slow recompaction of the sand layer occurs ($t_2 < t < t_3$) until a steady compacted state is reached ($t > t_3$). The white vertical rectangle gives a scale of 0.2 cm and $d = 110 \mu\text{m}$.

In the present experiment, the viscous length $l_v = 55 \mu\text{m}$ is kept constant, while the others length scales A , d , and δ are varied by a large amount. Combining these quantities, we construct three independent dimensionless numbers: $\text{Re}_\delta = U\delta/\nu = 2A/\delta$, $\text{Re}_d = Ud/\nu = 2Ad/\delta^2$, and $F_d = \rho_f^{1/2}U/((\rho_s - \rho_f)gd)^{1/2} = 2Al_v^{3/2}/(\delta^2 d^{1/2})$. The value reached by the Stokes Reynolds number, $\text{Re}_\delta = 40\text{--}500$, is relatively small and below the fully turbulent regime (100) for almost all cases [16]. The fluid boundary layer is then expected to be laminar or weakly disturbed. Besides, the Froude number $F_d = 2\text{--}10$ reaches small values close to the marginal limit ($F_d \approx 2$) obtained from linear stability analysis (Fig. 9 of Ref. [2] for $\text{Re}_d = 20\text{--}60$).

To measure the ripple dynamics, we stopped the oscillation of the cell at regular intervals, 30 or 60 oscillations for instance. The sand pattern remains, even with no flow oscillations. Then, the annular cell was driven in a very slow rotation and we recorded the sand-fluid interface from the outer transparent cylinder with a macro zoom and a charge-coupled device camera. This procedure gives an extremely high spatial resolution: $20 \mu\text{m}$ for the vertical direction and $200 \mu\text{m}$ for the horizontal one.

We have noticed that the preparation of the sand bed may have a drastic influence on the first measured wavelength. To flatten initially the sand bed, we oscillate the cell at high frequency and get a superficial fluidization of the granular layer. We observed strong variations (30% dispersion) of the initial ripple wavelength just by changing the duration and the intensity of the flattening procedure. We suspect here the influence of the internal structure and the local compaction of the granular material. In order to avoid such dispersion and obtain reproducible results, we fixed the flattening procedure as follows. A typical evolution of the sand layer height, during this initial preparation, is shown in Fig. 1. In the first stage ($t < t_1$) we oscillated the cell at high frequency and high amplitude ($f = 3$ Hz and $A = 3$ cm) to get a complete fluidization of the upper sand layer and destroy all previous patterns. Then, we strongly decreased the amplitude

($A = 0.1$ cm) keeping a high frequency ($t_1 < t < t_2$). Afterwards ($t_2 < t < t_3$), due to the weak oscillations, the sand is slowly compacted until a flat final state is reached (at t_3). We stopped the oscillations when there is no more variation in the sand height ($t > t_3$).

Once we obtained this flat and compacted interface, we run the experiment. To get close to the onset of ripple formation, we decreased the amplitude of oscillation A for fixed values of δ and d . The corresponding temporal evolutions of the mean ripple wavelength λ , for $d = 110 \mu\text{m}$ and $\delta = 560 \mu\text{m}$, are plotted in Fig. 2(a). For a high amplitude [$A = 3.1$ cm, Fig. 2(a)], rolling-grain ripples appears quickly after 20–30 oscillations. Then, the ripple wavelength increases rapidly due to the coarsening process. This latter leads to a final vortex ripples state. For a small amplitude [$A = 1.2$ cm, Fig. 2(a)], it took hundreds of oscillations before a first pattern, which fills the whole cell, could be detected. Afterwards, the system evolved on a longer time scale: hours or days.

Moreover, we noticed that given a grains size, the first measured wavelengths reached a constant value when A tends to be small for a constant frequency [Fig. 2(b)]. This is probably an evidence that the system gets close to its marginal stability limit as the time for the appearance of the pattern increases when the amplitude decreases. In addition, we changed the grains diameter and we recovered the same behavior with the difference that the threshold amplitude for pattern formation increases with the grains size. Besides, if we plot the probability distribution function (pdf) of individual ripple wavelength among the whole sand pattern, here again, significant differences appear between low and high A [Fig. 2(c)]. For large amplitude of oscillation, the pdf exhibits asymmetry with a long tail for small wavelengths. This is the signature of few local merging events: the distance between neighboring ripples tends to zero during a merging. Therefore, we claim that the first measured wavelength can be identified with the unstable wavelength of the flat sand bed only in the weak forcing case (i.e., for small A). For a strong forcing, the unstable growth and the coarsening evolve on the same time scale and these two mechanisms affect the wavelength selection.

Similarly, given a constant amplitude, we noticed that the first measured wavelengths reached a constant value when the frequency f tends to be small that is when the Stokes layer δ tends to be large [Fig. 3(a)], once again close to the threshold for sediment movement and also for stability limit. For higher frequencies, coarsening appears and the wavelength increases. Changes in the frequency at constant amplitude induce a stronger acceleration of the coarsening than changes in the amplitude at constant frequency. It is consistent with the evaluation of Taylor for the movement threshold: he showed that, assuming laminar flow, the amplitude, the frequency, and the grain diameter are linked by the following constraint $Af^{3/2}/d = \text{const.}$ expressing that the shear force $\tau d^2 \sim \rho_f \nu V d^2 / \delta$ normalized by the reduced weight $(\rho_s - \rho_f)gd^3$ equals a constant close to the limit for movement [1,5]. More generally, a relationship exists between all the relevant length scales [$F(A, d, \delta, l_v) = 0$] close to threshold without assuming necessarily a laminar flow. As

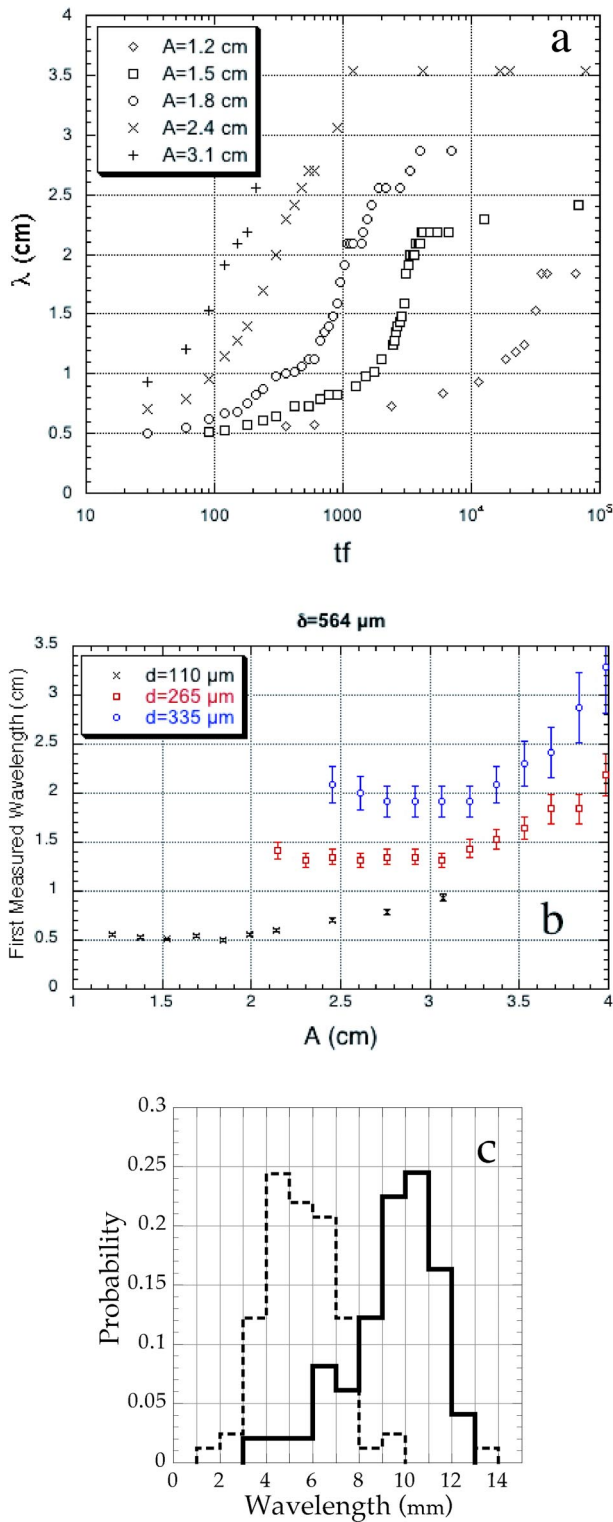


FIG. 2. (Color online) Influence of the amplitude of oscillation A on the ripple wavelength for fixed values of $d = 110 \mu\text{m}$ and $\delta = 564 \mu\text{m}$. Temporal evolution of the mean wavelength from $A = 1.2$ cm to 3.1 cm (a) and mean initial wavelength for $d = 110 \mu\text{m}$, $d = 265 \mu\text{m}$, and $d = 335 \mu\text{m}$ (b). For $d = 110 \mu\text{m}$ and $\delta = 564 \mu\text{m}$, the pdf of individual ripple wavelength (c) are given for weak ($A = 1.2$ cm in dashed line) and strong ($A = 3.1$ cm in solid line) forcing cases. The corresponding skewnesses are $S = +2.4$ and $S = -1$.

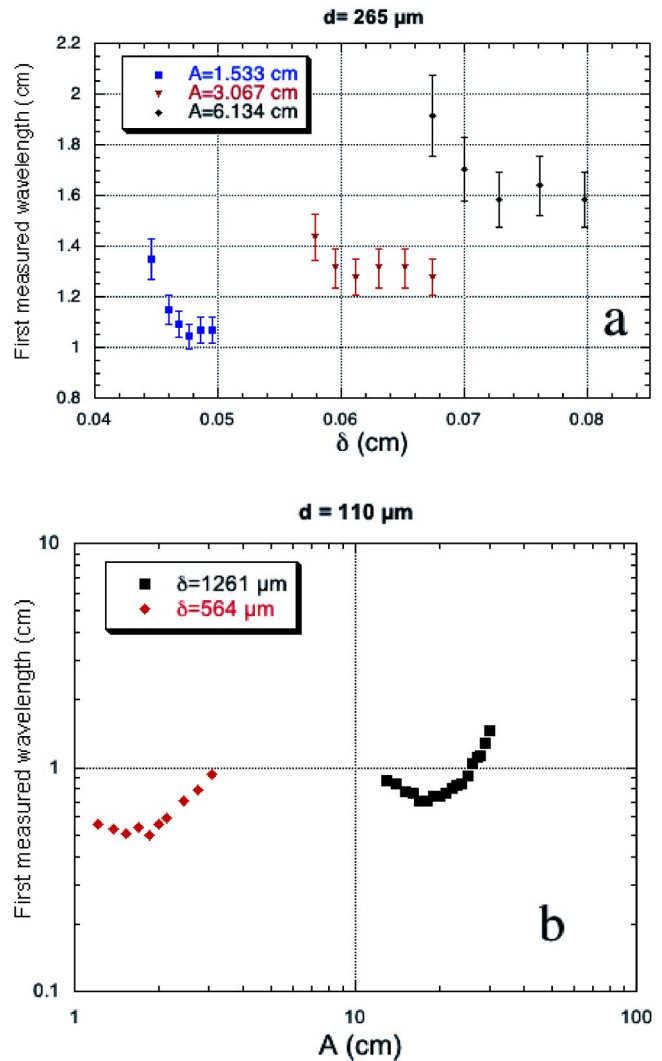


FIG. 3. (Color online) (a) Influence of the frequency of oscillation f on the ripple wavelength for different values of the amplitude $A = 1.5$ cm, $A = 3$ cm, and $A = 6$ cm for fixed values of $d = 265 \mu\text{m}$. (b) Mean initial wavelength for different values of the Stokes layer $\delta = 564 \mu\text{m}$ and $\delta = 1261 \mu\text{m}$ for fixed values of $d = 110 \mu\text{m}$.

before, we changed the amplitude and we recovered the same behavior with the difference that the threshold frequency for pattern formation decreases when the amplitude increases. Finally, for a constant grains diameter, we changed the amplitude and got close to the stability limit by diminishing it. Then, we changed the frequency and noticed the same behavior: the first measured wavelength tends to a constant [Fig. 3(b)]. A new setup with a larger gap ($a = 1.9$ cm) was built in order to perform the measurement for $\delta = 1261 \mu\text{m}$ and avoid boundary layer effect between the concentric cylinders. We have to mention that very close to the limit for pattern formation, some ripples may appear but we can hardly detect a pattern which fill the whole annulus (these situations are not reported here). It may also explain why there is a tendency to underestimate the number of ripples all around the perimeter that is to overestimate the mean initial wavelength when one gets close to the stability limit.

We have collected all the results concerning the first mea-

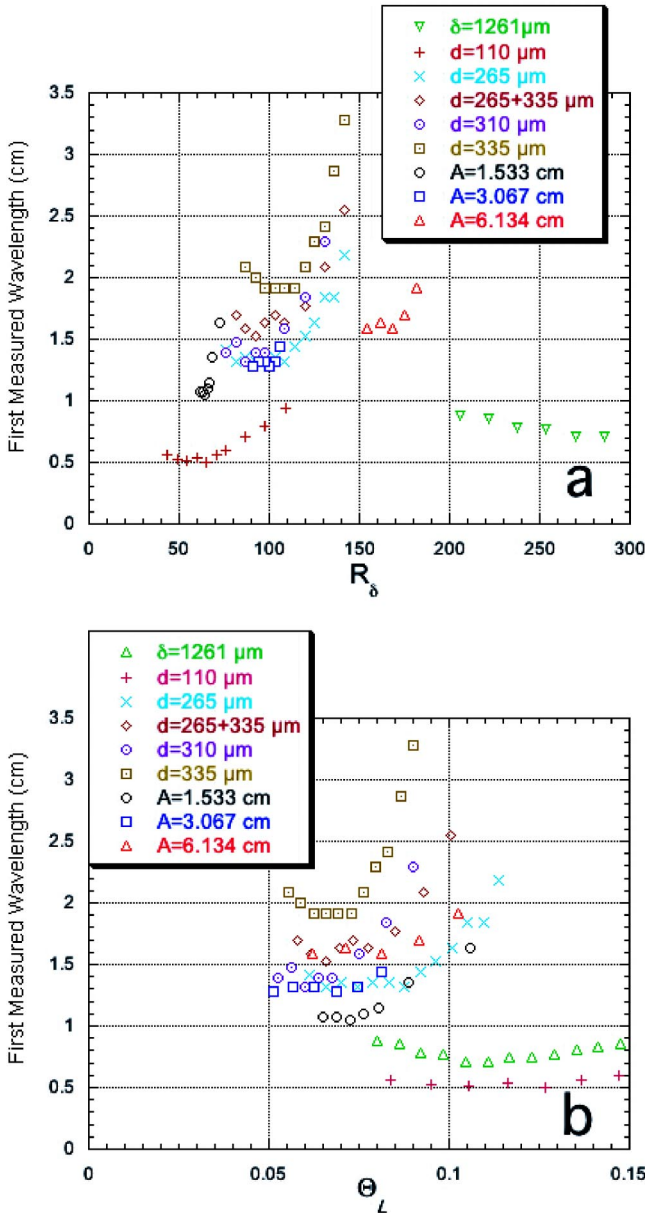


FIG. 4. (Color online) First measured wavelength in function of (a) the Reynolds number based on the Stokes layer R_δ and of (b) the laminar Shields number $\Theta_L = F_d^2/R_\delta$.

sured wavelength in function of some dimensionless numbers which do often appear in the morphology literature like the Froude number, its square that is the mobility number (not represented here), the Reynolds number based on the Stokes layer, and the laminar Shields number which is the ratio of the mobility number to the Reynolds number (Figs. 4 and 5). The representation in function of the Froude number is not far from the prediction of Blondeaux. We recover the critical value of marginal stability $F_d \sim 2$ for $R_d \sim 10-60$ (Fig. 9 of Ref. [2]). Nevertheless, the threshold of the rolling-grain ripples instability is controlled by more than one dimensionless parameter. In Fig. 6, we plot the value of F_d and R_δ close to the instability threshold when the first measured wavelength reaches a constant value. This curve gives an upper-bound limit to stable region. According to

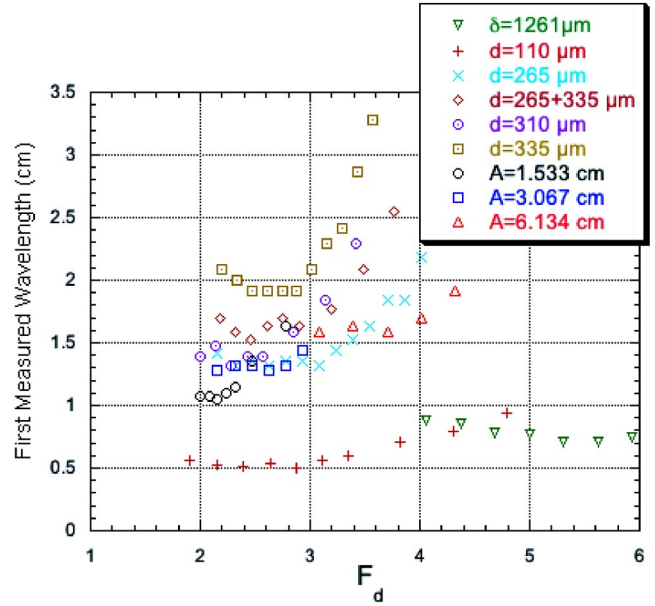


FIG. 5. (Color online) First measured wavelength in function of the Froude number F_d .

these results for weak $R_\delta \sim 50-100$, the critical Froude number F_d is almost constant. Hence, in this range of parameters, F_d seems to be the unique control parameter of the instability. However, for larger $R_\delta > 100$, one notices that the critical Froude number increases significantly with R_δ , namely, the instability threshold is fixed by both F_d and R_δ .

In order to investigate the influence of the Stokes layer δ and the grain size d on λ_0 , the marginal unstable wavelength of rolling grain ripples, we performed various experiment in the weak forcing regime. Unlike the equilibrium vortex ripple state which is almost independent of δ and d , here λ_0 increased both with δ and d (Fig. 7). For each grain size used $d=65 \mu\text{m}$, $110 \mu\text{m}$, $190 \mu\text{m}$, $265 \mu\text{m}$, $310 \mu\text{m}$, and $335 \mu\text{m}$, a large range of frequency was swept in order to

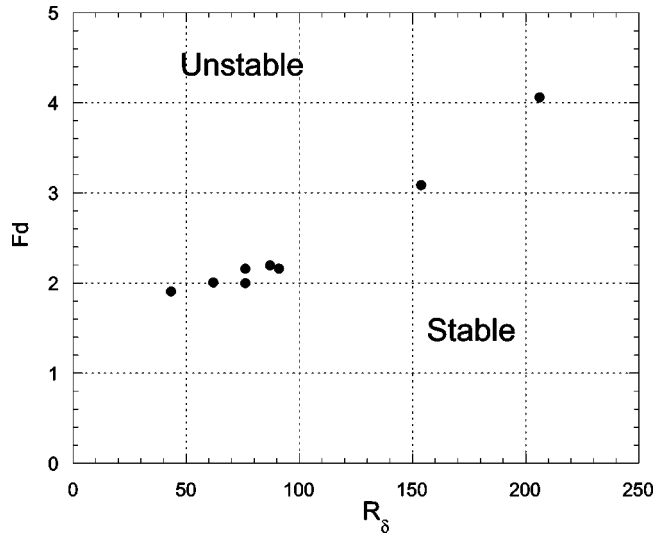


FIG. 6. Critical Froude number F_d in function of Stokes Reynolds number R_δ .

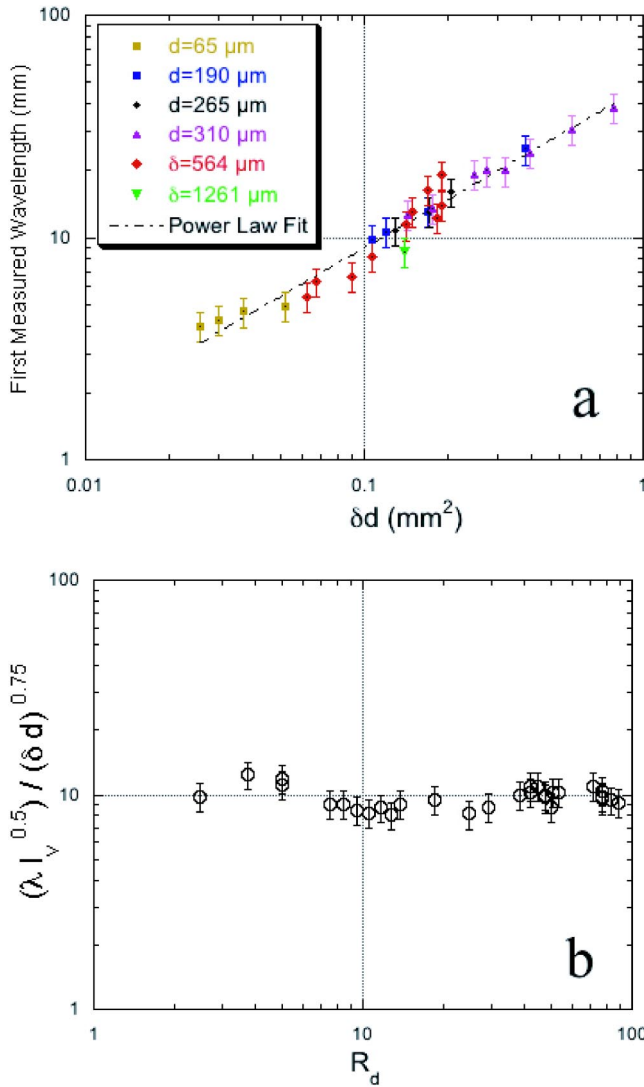


FIG. 7. (Color online) First measured wavelength in function of (a) $(\delta \cdot d)$ (the experimental power exponent is 0.72) and (b) first measured wavelength rescaled by $(\delta d)^{3/4} / \sqrt{l_v}$ in function of R_d .

study the ripple patterns for different values of the Stokes layer δ without forgetting that to be close to the threshold for instability we changed the amplitude. The best fit was obtained with a power law exponent $3/4$ for both d and δ where we have chosen d and δ as representative variables. Indeed, we could have plotted the result in function of the couple A , d or with the couple A , δ as the three parameters are linked by the constraint $F(A, d, \delta, l_v) = 0$. However, the representation with δ and d is more appropriate as the variation in amplitude must be important in order to observe significant differences with respect to d and δ . Then, to get a dimensionless wavelength, we needed to introduce a third length scale. According to the dimensional analysis of the system, the viscous length l_v is the only one left. Hence, even if l_v is kept constant in our investigations, we suggest the following relation $\lambda_0 \sim (\delta d)^{0.75} l_v^{-0.5}$ [Fig. 7(a)]. This indicative scaling is in good agreement with the experimental results for almost two decades of $Re_d = 3 - 100$ [Fig. 7(b)].

In addition to the wavelength selection, an important issue

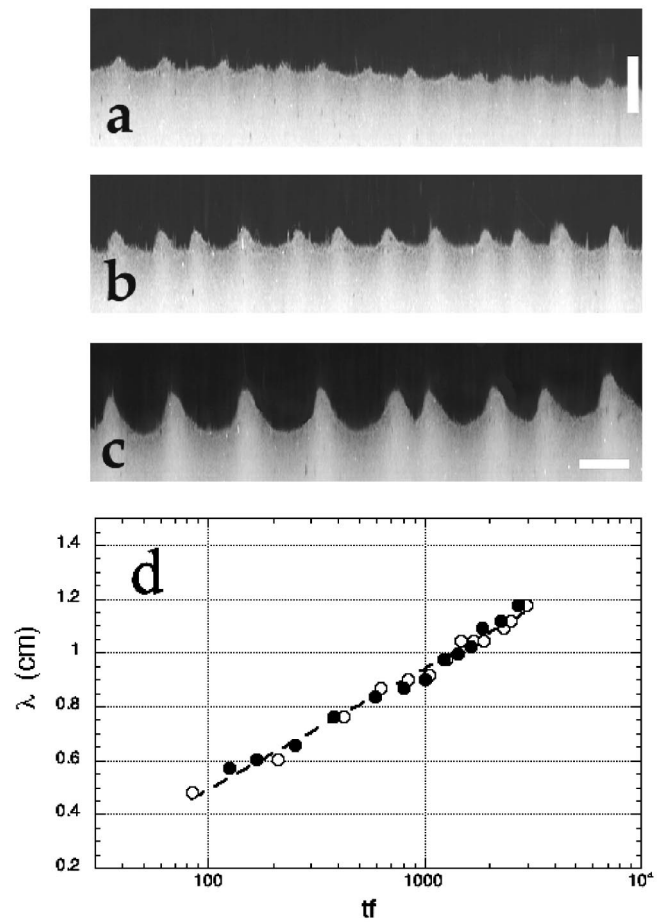


FIG. 8. (Color online) Morphological evolution of rolling-grain ripples during the coarsening process for $A=2.4$ cm, $\delta=670 \mu\text{m}$, $d=110 \mu\text{m}$. Ripple shape after 120 (a), 600 (b), and 2700 (c) oscillations. The white rectangles give a vertical scale of 1 mm on picture (a) and a horizontal scale of 1 cm on picture (c). Corresponding evolution of the mean ripple wavelength with semilog axis (d). Open and full circles correspond to two different experiments.

of this study is to characterize the dynamical and morphological evolution of the ripples during the coarsening process. In the first stage of growth (100 oscillations for the present case) the ripple height did not exceed three or four grain diameters [Fig. 8(a)]. At this stage, the maximum angle of the pattern was around 7° , well below the avalanche angle of the granular material. Then, ripples slowly merged together and both their height h and the maximum angle α increased: for instance $h \approx 0.04$ cm, $\alpha = 9^\circ - 14^\circ$ for 600 oscillations [Fig. 8(b)] and $h \approx 0.075$ cm, $\alpha = 14^\circ - 19^\circ$ for 2700 oscillations [Fig. 8(c)]. The rolling-grain ripples never reached a morphological equilibrium, and after 3000 oscillations (for the present case), high amplitude ripples appeared in the domain and the system evolved abruptly to a final vortex ripples state. Hence, there is no self-similarity of the ripple shape during the coarsening process and, at all times, they strongly differ from sinusoidal patterns.

Recently, several amplitude equations, satisfying the symmetries of the sand-fluid system, have been proposed to describe various ripple dynamics [18,19]. These models always

show a coarsening of the structures and in some cases they predict a logarithmic growth of the wavelength. Experimental validation of such a behavior is always difficult because it requires a significant evolution of the wavelength for a long time. However, in a few cases, close to the onset of ripple formation, these conditions were satisfied in our experiments and we have found that the coarsening of rolling grain ripples follows a logarithmic growth [Fig. 8(d)]. Nevertheless, the distinction between a logarithmic law or a weak power law cannot be done with this data set.

In conclusion, to understand the rolling-grain ripples dynamics (and analyze the experimental results) a clear distinction should be made between the initial formation of ripples (resulting from the flat sand bed instability) and the ripple coarsening which follows. According to the large numbers of experiments and the restricted conditions to obtain the initial

wavelength, we can propose an indicative law for the wavelength selection which is a function of d , δ , and l_v . Our data show that for small $R_\delta \sim 50-100$, the Froude number F_d is the main control parameter of the instability. However, for larger R_δ , the instability threshold is given by both F_d and R_δ . The values of F_d and R_δ for the marginal stability limit predicted in Ref. [2] is in reasonable agreement with our results. Besides, we were able to follow with a great accuracy the morphological evolution of the ripple during the coarsening process. During this stage, the ripple steepness increased with time and, in specific cases, we observed a logarithmic coarsening of the rolling-grain ripples.

We are grateful to K. H. Andersen, F. Charru, and F. Marin for enlightening discussions. This work was supported by the A.C.I. "Jeunes chercheurs" No. 2314.

-
- [1] R.A. Bagnold (with an additional note by G.I. Taylor), Proc. R. Soc. London, Ser. A **187**, 1 (1946).
- [2] P. Blondeaux, J. Fluid Mech. **218**, 1 (1990).
- [3] T. Gerkema, in Proceedings of Physics of Estuaries and Coastal Seas '96 by J. Dronkers and M. Scheffers, pp. 387-395, ISBN Report No. 9054109653, 1998.
- [4] K.H. Andersen, Phys. Fluids **13**, 58 (2001).
- [5] M.A. Scherer, F. Melo, and M. Marder, Phys. Fluids **11**, 58 (1999).
- [6] A. Stegner and J.E. Wesfreid, Phys. Rev. E **60**, R3487 (1999).
- [7] C. Faraci and E. Foti, Phys. Fluids **13**, 1624 (2001).
- [8] M.S. Longuet-Higgins, J. Fluid Mech. **107**, 1 (1981).
- [9] W.H. Lyne, J. Fluid Mech. **50**, 33 (1971).
- [10] J.F.A. Sleath, J. Hydraul. Res. **14**, 69 (1976).
- [11] A. Kaneko and H. Honji, J. Fluid Mech. **93**, 727 (1979).
- [12] L. Petit and P. Gondret, J. Phys. II **2**, 2115 (1992).
- [13] A. Betat, V. Frette, and I. Rehberg, Phys. Rev. Lett. **83**, 88 (1999).
- [14] A. Betat, C.A. Kruehle, V. Frette, and I. Rehberg, Eur. Phys. J. E **8**, 465 (2002).
- [15] A. Aouidef, C. Normand, A. Stegner, and J.E. Wesfreid, Phys. Fluids **6**, 3665 (1994).
- [16] B.L. Jensen, B.M. Sumer, and J. Fredsoe, J. Fluid Mech. **206**, 265 (1989).
- [17] J. Lundbeck Hansen *et al.*, Nature (London) **410**, 324 (2001).
- [18] P. Politi, Phys. Rev. E **58**, 281 (1998).
- [19] Z. Csahok *et al.*, Eur. Phys. J. E **3**, 71 (2000).